Featured in Physics

# Geometric Mechanics of Origami Patterns Exhibiting Poisson's Ratio Switch by Breaking Mountain and Valley Assignment

Phanisri P. Pratapa,* Ke Liu,* and Glaucio H. Paulino†
*School of Civil and Environmental Engineering, Georgia Institute of Technology, Atlanta, Georgia 30332, USA*

(Received 14 September 2018; published 19 April 2019)

Exploring the configurational space of specific origami patterns [e.g., Miura-ori (flat surface with parallelogram crease patterns), eggbox] has led to notable advances in science and technology. To augment the origami design space, we present a pattern, named "Morph," which combines the features of its parent patterns. We introduce a four-vertex origami cell that morphs continuously between a Miura mode and an eggbox mode, forming an homotopy class of configurations. This is achieved by changing the mountain and valley assignment of one of the creases, leading to a smooth switch through a wide range of negative and positive Poisson's ratios. We present elegant analytical expressions of Poisson's ratios for both in-plane stretching and out-of-plane bending and find that they are equal in magnitude and opposite in sign. Further, we show that by combining compatible unit cells in each of the aforementioned modes through kinematic bifurcation, we can create hybrid origami patterns that display unique properties, such as topological mode locking and tunable switching of Poisson's ratio.

DOI: 10.1103/PhysRevLett.122.155501

Origami-inspired geometries have been used to design metamaterials with unusual properties [1–7]. The aesthetically pleasant patterns and shapes typically start from 2D sheets to construct 3D structures according to mountain and valley assignments encoded in the crease patterns. In this Letter, we present a new periodic pattern, named Morph, with a nondevelopable degree-4 unit cell that allows a certain crease to switch its mountain and valley assignment, leading to properties such as an arbitrarily tunable Poisson's ratio that spans from positive to negative and topological mode locking.

Owing to their special geometries, origami metamaterials usually display interesting behavior [8–11]. For instance, the Miura-ori exhibits a negative Poisson's ratio under in-plane deformations [9], while the standard eggbox pattern has a positive Poisson's ratio [12,13]. In comparison, our proposed pattern morphs continuously between a Miura mode and an eggbox mode (see Fig. 1), thus behaving as a single material possessing both positive and negative Poisson's ratio. Poisson's ratio switching is an enticing phenomenon that has only been found recently for selected mechanical metamaterial designs, including nanoplates [14], reentrant origami tube assemblages [15], bistable auxetics [16], kirigami structures [17], and soft networks [18]. Compared to other designs, the Morph excels on having a wider tunable range of Poisson's ratio, theoretically from negative infinity to positive infinity. In addition, the Morph unit cells can be assembled to form 2D tessellations in which the unit cell can stay either in the Miura or eggbox mode, which allows the formation of hybrid patterns—achieved by harnessing kinematic bifurcation.

In their most general form, the panel angles $\alpha$ and $\beta$ of the Morph pattern are two independent geometric parameters (see Fig. 1), thereby enriching the origami design space, unlike the standard cases such as eggbox ($\beta = \alpha$) or Miura-ori ($\beta = \pi - \alpha$) whose vertex geometry is dictated by just a single parameter $\alpha$. Additionally, for $\alpha \neq \beta$, the degree-4 nondevelopability feature that the Morph shares with the standard eggbox makes it a generalization of the basic pattern. Theoretically, Poisson's ratio of the Morph sweeps the whole spectrum of real numbers as it morphs from one flat-folded state to the eggbox mode, to the Miura mode, and to another flat-folded state, as shown in Fig. 1. The red crease in Fig. 1 changes its mountain and valley assignment as it *transitions* from eggbox mode to the Miura mode, which is made possible owing to the fact that the angle $\beta$ is smaller than the angle $\alpha$ of the other two panels. By contrast, the standard eggbox or Miura-ori patterns do not allow any crease to switch its mountain and valley assignment.

To parametrize the rigid origami behavior of the Morph unit cell, we define angles $\phi$, $\psi$ as the angles between opposing crease lines and denote the dihedral angles between the panels as $\gamma_1$, $\gamma_2$, $\gamma_3$, $\gamma_4$, as shown in Fig. 2(a). The unit cell has a degree-4 vertex, and thus it is a single degree of freedom system. The dihedral angles are related to one another and to $\phi$, $\psi$. We derive that $\gamma_2 = \gamma_4$, as $0 \leq \gamma_2, \gamma_4 \leq \pi$, indicating the existence of a plane of symmetry passing through the vertices denoted by $O_4$, $O_5$,

 

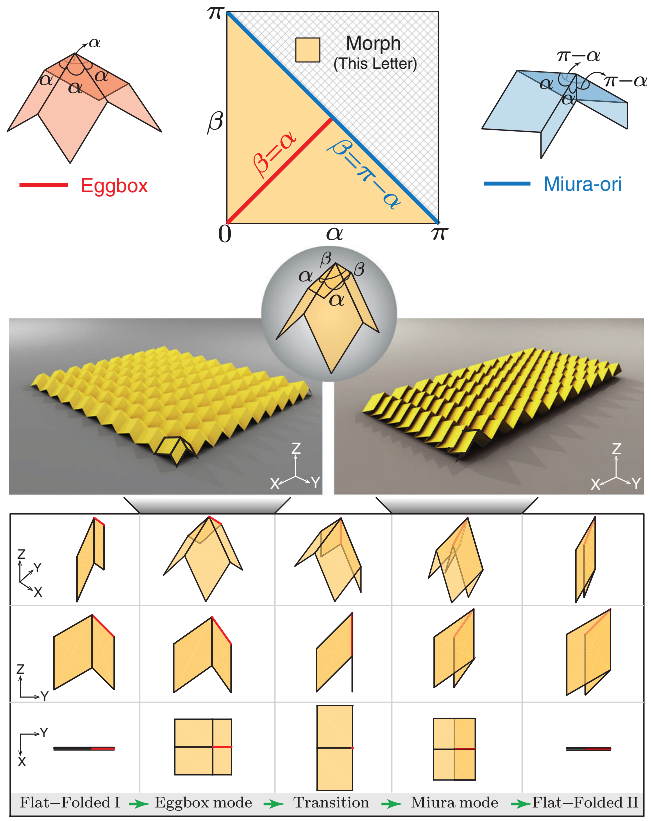


FIG. 1. (Top) Expanded design space of the Morph pattern (yellow shading) with standard eggbox (red line) and Miura-ori (blue line) as particular cases. (Middle) Fundamental modes of the Morph pattern: eggbox mode (left) and Miura mode (right). (Bottom) Configuration space showing transition of the Morph unit cell from one flat-folded state to another (see Supplemental Video 1). The crease line shown in red morphs from a mountain fold in the eggbox mode to a valley fold in the Miura mode.

and $O_6$. While $0 \leq \gamma_1 < \pi$, the ability of the crease $O_5O_6$ to switch between mountain and valley allows $\gamma_3$ to vary from 0 to $2\pi$. In the flat-folded state I, $\phi = \phi_{\max} = \alpha + \beta$ and $\gamma_3 = 0$. For $0 < \gamma_3 < \pi$, the unit cell is in eggbox mode and $O_5O_6$ is a mountain crease. As $\gamma_3$ passes through $\pi$, $O_5O_6$ transitions from a mountain to a valley crease and the panels on either side of $O_5O_6$ become coplanar. In the transition state, angle $\psi$ also reaches its maximum $\psi_{\max} = 2\beta$. For $\pi < \gamma_3 < 2\pi$, the unit cell is in Miura mode and $O_5O_6$ is a valley crease. Finally, as $\gamma_3 \to 2\pi$, the unit cell approaches the flat-folded II state with $\phi = \phi_{\min} = \alpha - \beta$. Let us define two intermediate variables

$$\xi = \cos\beta - \cos\alpha\cos\phi = \sin\alpha\sin\phi\cos(\gamma_1/2), \quad (1)$$

$$\zeta = \cos\alpha - \cos\beta\cos\phi = \sin\beta\sin\phi\cos(\gamma_3/2). \quad (2)$$

The configurational space of the Morph unit cell is then fully described by $\phi$ $(0 \leq \psi \leq 2\beta < \pi)$ and $\psi$ $(0 < \alpha - \beta \leq \phi \leq \alpha + \beta < \pi)$ through the following equation:

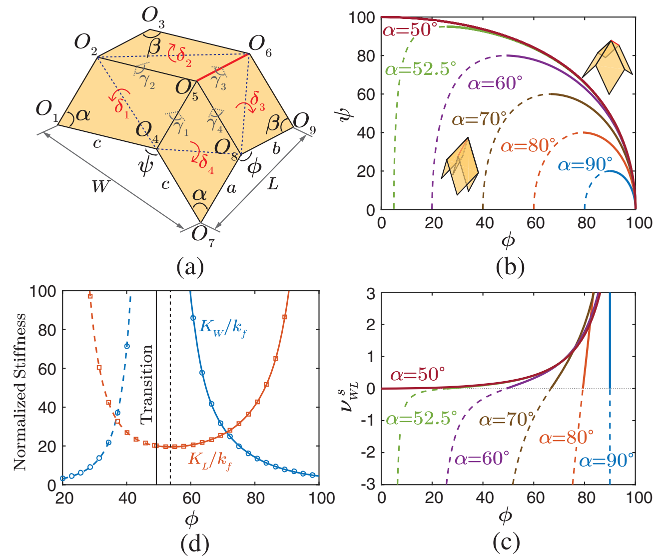


FIG. 2. Geometric configuration and in-plane mechanics of the Morph pattern. (a) Schematic of the unit cell with the description of geometric parameters and vertices. (b),(c) The configuration space and Poisson's ratio in stretch, respectively, for different choices of $\alpha$ considering $\alpha + \beta = 100°$. The solid and dashed lines represent the eggbox and Miura modes, respectively. (d) Stretching stiffness in **W** and **L** directions for $\alpha = 60°$, $\beta = 40°$. The markers represent numerical results from origami structural analyses using the bar-and-hinge reduced-order model [19]. We assume that $a = c = 1$.

$$\cos\psi = \cos 2\alpha + 2\xi^2 \csc^2\phi, \quad (3)$$

which is presented for various choices of panel angles in Fig. 2(b). We can observe in Fig. 2(b) that, as $\alpha \to \beta$, the Miura mode vanishes.

We define Poisson's ratio for in-plane stretching as the tangential ratio of the orthogonal strains measured by the change of width $W$ and length $L$ of a unit cell [8,9], which are given by

$$W = 2c\sin(\psi/2), \qquad L = \sqrt{a^2 + b^2 - 2ab\cos\phi}. \quad (4)$$

To assure the bounding box of a unit cell being orthorhombic, which requires, for example, $(O_1\,O_4\,O_7) \perp (O_1\,O_7\,O_9\,O_3)$ and $(O_1\,O_2\,O_3) \perp (O_1\,O_7\,O_9\,O_3)$, the panel dimensions $a$ and $b$ are constrained by $b = a|\cos\alpha/\cos\beta|$ (see Sec. I of the Supplemental Material [20]). The analytical expression for the in-plane Poisson's ratio when stretching in the **L** direction is

$$\nu^s_{WL} = -\frac{dW/W}{dL/L} = \frac{4c^2L^2}{a^2W^2}\left|\frac{\cos\beta}{\cos\alpha}\right|\frac{\xi\zeta}{\sin^4\phi}. \quad (5)$$

As plotted in Fig. 2(c), it is clear that the stretching Poisson's ratio is negative in the Miura mode and positive in the eggbox mode, with a smooth transition near zero.

Theoretically, $\nu_{WL}^{s}$ approaches $-\infty$ or $+\infty$ in the two flat-folded limits, thereby leading to a wide range of tunability. We note that, since $W^2/c^2$ and $L^2/a^2$ do not depend on the length dimensions of the unit cell, Poisson's ratio of the unit cell depends only on $\alpha$, $\beta$, and $\phi$, making it a purely geometric quantity that is also independent of the length scale of the pattern.

Accordingly, assuming that the energy of the unit cells is composed of deformation from linear elastic rotational hinges along the crease lines, we can derive the linear in-plane stretching stiffness of the pattern. Denoting $k_f$ as the rotational spring modulus, the stored energy of the system is given by

$$\mathcal{U}_s = \frac{k_f}{2}[a(\gamma_1-\gamma_{1,0})^2 + b(\gamma_3-\gamma_{3,0})^2 + 2c(\gamma_2-\gamma_{2,0})^2], \tag{6}$$

where $\gamma_{1,0}$, $\gamma_{2,0}$, and $\gamma_{3,0}$ are the neutral dihedral angles (in the undeformed state). Expressing $\gamma_2$ and $\gamma_3$ in terms of $\gamma_1$, the stiffnesses along the $\mathbf{L}$ direction is derived as

$$K_L = \frac{d^2\mathcal{U}_s}{dL^2}\bigg|_{L=L_0} = \frac{d^2\mathcal{U}_s}{d\gamma_1^2}\left(\frac{dL}{d\phi}\frac{d\phi}{d\gamma_1}\right)^{-2}\bigg|_{\gamma_1=\gamma_{1,0}}. \tag{7}$$

Similarly, we can get the stiffness along the $\mathbf{W}$ direction (see Sec. II of the Supplemental Material [20]). As shown in Fig. 2(d), the in-plane stiffness in the $\mathbf{W}$ direction (denoted by $K_W$) is minimum at flat-folded states and reaches maximum at the transition state. Interestingly, while $K_L$ is maximal at flat-folded states, it is only close to minimum at the transition but slightly away towards the eggbox mode.

As revealed in previous research [8,9,12], a kinematically single degree of freedom (d.o.f.) origami pattern may experience out-of-plane deformation, other than pure (in-plane) folding, if compliance of panels is taken into consideration. Accordingly, we define Poisson's ratio in bending as the ratio of principal curvatures ($\nu_{WL}^{b} = -\kappa_W/\kappa_L$) and find that the Morph pattern features a saddle-shaped geometry in the Miura mode and a dome-shaped geometry in the eggbox mode [see Figs. 3(a) and 3(b)]. It is intriguing that the Morph pattern exhibits distinct Poisson's ratio in stretching and bending, similar to what have been found, separately, with the standard Miura-ori and the standard eggbox patterns. Here we show that, just like its two extreme cases [9,12], the Morph pattern displays Poisson's ratio with opposite sign but equal magnitude in stretching and bending. We can analytically calculate the principal bending curvatures by allowing each panel of the origami pattern to bend along one of its diagonals [9], under the assumption of infinitesimal deformation.

We add infinitesimal rotations $\delta_1$, $\delta_2$, $\delta_3$, $\delta_4$ as shown in Fig. 2(a) to provide further degrees of freedom to the system in order to simulate bending of panels. Hence, there are in total four extra degrees of freedom being added, yet isometric deformation is still ensured. Bending of the unit cell shall preserve the orthogonality between the two sides of a unit cell (i.e., $\mathbf{L}$ and $\mathbf{W}$). Thus, we enforce that the normals of the side triangles of a unit cell after bending [e.g., $\Delta(O_1' O_2' O_3')$, $\Delta(O_7' O_8' O_9')$, $\Delta(O_1' O_4' O_7')$, $\Delta(O_3' O_6' O_9')$] remain orthogonal to their respective side directions, which leads to three independent constraints,

$$a\xi\frac{\delta_1}{\ell_1} = b\zeta\frac{\delta_2}{\ell_2}, \qquad b\zeta\frac{\delta_3}{\ell_3} = a\xi\frac{\delta_4}{\ell_4}, \qquad \frac{\delta_1}{\ell_1} = \frac{\delta_4}{\ell_4}, \tag{8}$$

where $\ell_1$, $\ell_2$, $\ell_3$, and $\ell_4$ are the lengths of the diagonals $O_2O_4$, $O_2O_6$, $O_6O_8$, and $O_4O_8$, respectively. Thus, the bending is uniquely defined up to a single d.o.f. These constraints automatically ensure that the deformed unit cell can be periodically tessellated in the two principal directions (i.e., $\mathbf{L}$ and $\mathbf{W}$), that is, $\angle(O_1' O_2' O_3') = \angle(O_7' O_8' O_9')$ and $\angle(O_1' O_4' O_7') = \angle(O_3' O_6' O_9')$.

The curvatures in $\mathbf{L}$ and $\mathbf{W}$ directions are determined by

$$\kappa_L = -\frac{|\theta_{147}| \pm |\theta_{369}|}{L}, \tag{9}$$

$$\kappa_W = -\frac{|\theta_{789}| + |\theta_{123}|}{W}, \tag{10}$$

where the $+$ or $-$ in Eq. (9) for $\kappa_L$ depends on whether the system is in the eggbox mode or the Miura mode, respectively, and $\theta_{147}$, $\theta_{369}$, $\theta_{789}$, and $\theta_{123}$ are the tilt angles

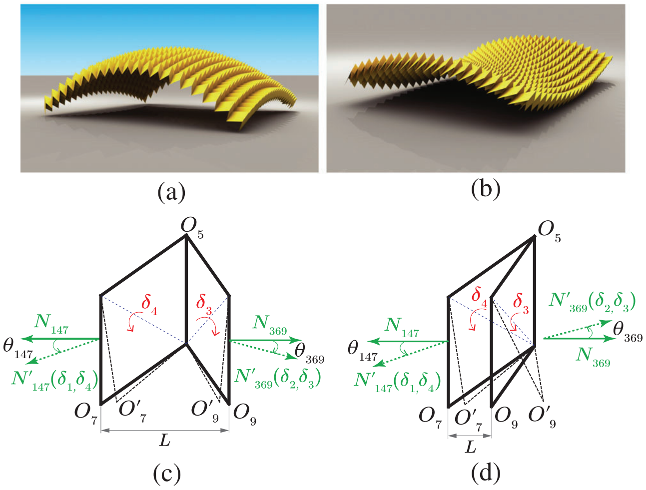


FIG. 3. Out-of-plane bending of the Morph pattern. (a),(b) Bent shapes of the pattern in eggbox and Miura modes, respectively, obtained using the bar-and-hinge origami model. (c),(d) Triangular face tilts creating a net angle change across length $L$ of the Morph pattern in eggbox and Miura modes, respectively. The new coordinates of vertices $O_7$ and $O_9$ after bending (i.e., $O_7'$ and $O_9'$, respectively) can be calculated using the Rodrigues rotation formula [21].

[see Figs. 3(c) and 3(d)]. The bending Poisson's ratio is then obtained as (see Secs. III and IV of the Supplemental Material [20])

$$\nu_{WL}^{b} = -\frac{\kappa_W}{\kappa_L} = -\frac{4c^2L^2}{a^2W^2}\left|\frac{\cos\beta}{\cos\alpha}\right|\frac{\xi\zeta}{\sin^4\phi}. \qquad (11)$$

Comparing Eq. (5) with Eq. (11), we obtain the elegant result $\nu_{WL}^{b} = -\nu_{WL}^{s}$ for the Morph pattern. The above expression reduces to standard Miura-ori [8,9] and eggbox [12] cases as two particular cases for appropriate choices of panel angles $\alpha$ and $\beta$ (see Secs. V and VI of the Supplemental Material [20]).

The aforementioned bending mode allows us to analytically derive the bending stiffness of the Morph pattern, which has similar characteristics to the in-plane stretching stiffness (see Fig. S8 of the Supplemental Material [20]). By performing numerical simulation using the reduced-order bar-and-hinge model [19], we find that the analytical model agrees well with the numerical simulations with very small discrepancies, which further strengthens the assumption that infinitesimal rotations about panel diagonals are sufficient to characterize first-order bending response of the Morph pattern.

Owing to its mode switching feature, the Morph pattern unit cells do not have to be tessellated with uniform configuration. It is kinematically admissible to couple the Morph unit cells into a *hybrid* pattern, such that there are both Miura mode cells and eggbox mode cells in a single tessellation, as demonstrated in Figs. 4(a) and 4(b). The feasibility of such a system can be understood by noting that, in Fig. 2(b), a given $\psi$ can correspond to the angle $\phi$ in either the eggbox mode or the Miura mode, which we denote as $\phi_e$ or $\phi_m$, respectively. These angles are given by $\phi_e = \phi_1 + \phi_2$ and $\phi_m = \phi_1 - \phi_2$, where $\phi_1$ and $\phi_2$ are as shown in Fig. 4(c) and are given by $\cos\phi_1 = \cos\alpha/\cos(\psi/2)$ and $\cos\phi_2 = \cos\beta/\cos(\psi/2)$ (see Sec. VII of the Supplemental Material [20]).

In Fig. 4(c), we show that one can smoothly deform a homogeneous Morph pattern to a hybrid pattern using rigid origami motion (no panel bending). By compatibility, all the unit cells have the same $\psi$, i.e., $\psi_m = \psi_e = \psi$. Also, when $\phi_m = \phi_e$, all the unit cells of the pattern are either in the Miura mode or the eggbox mode, depending on whether $\phi = \phi_m = \phi_1 - \phi_2$ or $\phi = \phi_e = \phi_1 + \phi_2$, respectively. In the figure, these configurations are represented by the straight line in blue and red colors, respectively. As we move up the blue line, the $\phi_m$ increases and reaches the transition point [which is $\phi_T = \cos^{-1}(\cos\alpha/\cos\beta)$] between Miura and eggbox modes. At this point, we note that there is kinematic bifurcation in the configuration space, which could either move all the unit cells into the eggbox mode by uniformly increasing the angle $\phi$ further across all cells or switch some of the strips back into Miura mode and therefore generate hybrid patterns represented by the green curve in the figure. This process is also demonstrated through animations and partly through physical testing in Videos 2 and 4, respectively, of the Supplemental

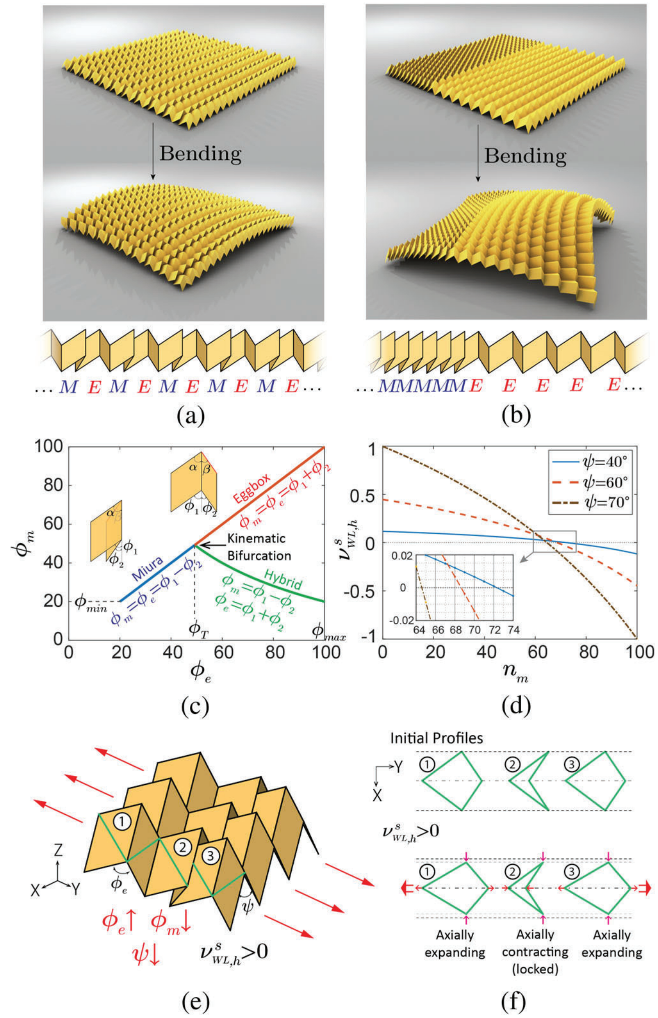


FIG. 4. Hybrid origami assemblages associated with the Morph pattern. (a) Alternating strips of Miura ($M$) and eggbox ($E$) modes. (b) Half pattern with strips in Miura ($M$) mode and the other half in eggbox ($E$) mode. (c) Creation of hybrid patterns from the Morph through kinematic bifurcation. (d) Change of Poisson's ratio with respect to varying number of Miura mode strips ($n_m$) in a hybrid mode with $100 \times 100$ unit cells. The notation $\nu_{WL,h}^{s}$ denotes Poisson's ratio under stretch for the hybrid pattern. (c),(d) We assume $\alpha = 60°$, $\beta = 40°$. (e),(f) Mode locking due to extension in **L** direction when $\nu_{WL,h}^{s} > 0$. The positive global Poisson's ratio implies contraction in the **W** direction, resulting in decrease of $\psi_e$ and $\psi_m$. The oppositely signed unit cell Poisson's ratios of the two modes indicates that while $\phi_e$ increases, $\phi_m$ decreases, meaning the Miura mode cells are axially contracting, opposite to the global axial deformation. The Miura mode cells with decreasing $\phi_m$ are locked because such cells can no longer smoothly transition to their eggbox mode in a rigid origami motion. (f) Contrasting global and local deformations that occur in hybrid patterns leading to mode-locking behavior. (e),(f) The green lines represent the panel diagonals, whose projections provide a clean way of sketching the motions.

Material [20]. It can be seen that, along the green curve, $\phi_m$ reduces and $\phi_e$ increases, as to be expected from Fig. 2(b), for a compatible $\psi$, across the two types of unit cells in the system.

Depending on the coupling mode of the hybrid pattern, the tessellated sheet exhibits a different Poisson's ratio, $\nu^s_{WL,h}$ [see Eq. (S98) of the Supplemental Material [20] ]. There exists a transition point when $\nu^s_{WL,h}$ varies from positive extremum (all unit cells in eggbox mode) to negative extremum (all unit cells in Miura mode), which, however, does not happen when the number of Miura mode and eggbox mode strips are the same, due to unequal contributions from both modes. We consider a system with $100 \times 100$ cells and increase the number of Miura mode cells (in strips) along the $\mathbf{L}$ direction (denoted as $n_m$) from 0 to 100 [see Fig. 4(d)]. For a given pattern, the switching of Poisson's ratio can be tuned to occur at different fold angles by smoothly modifying the number of Miura mode strips in the system (see Sec. VII B of the Supplemental Material [20]), which renders the Morph pattern reprogrammable.

The hybrid patterns also exhibit interesting behavior in bending due to the combined action from Miura and eggbox mode cells (see Video 3 of the Supplemental Material [20]). For example, a hybrid pattern with alternating Miura and eggbox mode strips bends into a dome shape [Fig. 4(a)], whereas that with a set of Miura mode strips adjacent to one another bends into a complex geometry that has both saddle and dome shapes [Fig. 4(b)].

The interplay between the contrasting Poisson's ratios of the eggbox and Miura mode unit cells coupled with the global Poisson's ratio of the hybrid pattern leads to mode-locking behavior. The most obvious mode locking is the tensile mode locking (demonstrated in Video 1 of the Supplemental Material [20]). For certain types of hybrid modes, if we stretch the hybrid pattern along the $\mathbf{L}$ (axial) direction, the Miura mode cells, which normally would smoothly transition into eggbox mode under stretching, would rather lock themselves in Miura mode and fold toward flat-folded state II. Tensile mode locking happens when a hybrid pattern displays a positive Poisson's ratio globally, such that it shrinks in the lateral direction under stretching. For a Miura mode unit cell, this means that it must contract in the axial direction (as well as the lateral direction), despite the fact that the global pattern is expanding in the axial direction in which it is stretched, as illustrated in Fig. 4(f). Similarly, compressive mode locking happens to eggbox unit cells when a hybrid pattern with globally negative Poisson's ratio is contracted (see Sec. VII C of the Supplemental Material [20]). We remark that the mode locking of a hybrid Morph pattern is topological. It locks the mountain and valley assignment of certain unit cells, but still allows the pattern to fold smoothly as a rigid origami to the flat-folded states. This is different from motion locking [22] where the panels come into contact with each other, hindering the rigid foldability and preventing the pattern from reaching the flat-folded state.

The Morph pattern exhibits morphing characteristics by breaking the mountain and valley assignment, which leads to smooth switching of Poisson's ratio across a very wide range of negative to positive values and topological mode locking as a consequence of kinematic bifurcation. Our analysis reveals that the Morph pattern exhibits Poisson's ratio with equal magnitude but opposite sign when subject to in- and out-of-plane deformations. Moreover, we discuss hybrid patterns that can be created by coupling Morph unit cells in distinct modes, creating a tessellation with reprogrammable Poisson's ratio and topological mode locking. The locking feature of the hybrid patterns can be useful in creating structures with multistability [3]. We envision that hybrid patterns can also have many applications in topological mechanics due their ability to transform the symmetry of the system under in-plane deformations [23,24].

We acknowledge useful discussions with Professor David Zeb Rocklin. We thank the support from the U.S. National Science Foundation (NSF) through Grant No. 1538830, the China Scholarship Council (CSC), and the Raymond Allen Jones Chair at Georgia Tech.

*P. P. P. and K. L. contributed equally to this work.
†Corresponding author.
paulino@gatech.edu

[1] J. T. Overvelde, J. C. Weaver, C. Hoberman, and K. Bertoldi, Nature (London) **541**, 347 (2017).
[2] E. T. Filipov, T. Tachi, and G. H. Paulino, Proc. Natl. Acad. Sci. U.S.A. **112**, 12321 (2015).
[3] S. Waitukaitis, R. Menaut, B. G.-g. Chen, and M. van Hecke, Phys. Rev. Lett. **114**, 055503 (2015).
[4] E. Boatti, N. Vasios, and K. Bertoldi, Adv. Mater. **29**, 1700360 (2017).
[5] S. Li, H. Fang, and K. W. Wang, Phys. Rev. Lett. **117**, 114301 (2016).
[6] J. L. Silverberg, A. A. Evans, L. McLeod, R. C. Hayward, T. Hull, C. D. Santangelo, and I. Cohen, Science **345**, 647 (2014).
[7] L. H. Dudte, E. Vouga, T. Tachi, and L. Mahadevan, Nat. Mater. **15**, 583 (2016).
[8] M. Schenk and S. D. Guest, Proc. Natl. Acad. Sci. U.S.A. **110**, 3276 (2013).
[9] Z. Y. Wei, Z. V. Guo, L. Dudte, H. Y. Liang, and L. Mahadevan, Phys. Rev. Lett. **110**, 215501 (2013).
[10] C. Lv, D. Krishnaraju, G. Konjevod, H. Yu, and H. Jiang, Sci. Rep. **4**, 5979 (2014).
[11] M. Eidini and G. H. Paulino, Sci. Adv. **1**, e1500224 (2015).
[12] H. Nassar, A. Lebée, and L. Monasse, Proc. R. Soc. A **473**, 20160705 (2017).
[13] M. Schenk, Folded shell structures, Ph. D. thesis, University of Cambridge, 2012.
[14] D. T. Ho, S.-D. Park, S.-Y. Kwon, K. Park, and S. Y. Kim, Nat. Commun. **5**, 3255 (2014).
[15] H. Yasuda and J. Yang, Phys. Rev. Lett. **114**, 185502 (2015).

[16] A. Rafsanjani and D. Pasini, Extreme Mech. Lett. **9**, 291 (2016).

[17] A. Rafsanjani and K. Bertoldi, Phys. Rev. Lett. **118**, 084301 (2017).

[18] J. Liu and Y. Zhang, Soft Matter **14**, 693 (2018).

[19] E. T. Filipov, K. Liu, T. Tachi, M. Schenk, and G. H. Paulino, Int. J. Solids Struct. **124**, 26 (2017).

[20] See Supplemental Material at http://link.aps.org/supplemental/10.1103/PhysRevLett.122.155501 for detailed derivations associated to the Morph pattern (geometry and configuration space of the Morph pattern, in-plane and out-of-plane behavior and Poisson's ratio; tessellations, hybrid patterns, stretch Poisson's ratio of hybrid patterns, and mode-locking during in-plane deformation).

[21] R. M. Murray, Z. Li, and S. S. Sastry, *A Mathematical Introduction to Robotic Manipulation* (CRC Press, Boca Raton, FL, 1994).

[22] H. Fang, S. Li, and K. W. Wang, Proc. R. Soc. A **472**, 20160682 (2016).

[23] B. G.-g. Chen, B. Liu, A. A. Evans, J. Paulose, I. Cohen, V. Vitelli, and C. D. Santangelo, Phys. Rev. Lett. **116**, 135501 (2016).

[24] D. Z. Rocklin, S. Zhou, K. Sun, and X. Mao, Nat. Commun. **8**, 14201 (2017).